

Eddy-mean flow interactions and vertical eddy energy redistribution associated with the standing meander in the Antarctic Circumpolar Current

Takuro Matsuta¹ and Yukio Masumoto²

¹The university of Tokyo

²University of Tokyo

November 26, 2022

Abstract

Recent studies suggest that local eddy-mean flow interactions associated with standing meanders play key roles in the dynamics of the

Antarctic Circumpolar Current. Here we explore the importance of the local dynamics quantitatively with a viewpoint of energy transfer using the Lorentz diagram concept. Results confirm the importance of the eddy-mean flow interactions in the standing meander, showing that 55% of the wind energy input is converted to the eddy energy through the baroclinic instability in the standing meander region. It is also found that most of the eddy kinetic energy is dissipated local in the deeper layer due to the vertical energy redistribution governed by the vertical pressure flux. Contrary, the eddy effects are negligible outside the standing meander region.

1 **Eddy-mean flow interactions and vertical eddy energy redistribution associated with**
2 **the standing meander in the Antarctic Circumpolar Current**

3 **Takuro Matsuta¹ and Yukio Masumoto^{1,2}**

4 ¹Department of Earth and Planetary Science, Graduate School of Science, the University of
5 Tokyo, Tokyo, Japan

6 ²Application Laboratory, Japan Agency for Marine-Earth Science and Technology, Yokohama,
7 Japan

8 Corresponding author: Takuro Matsuta (matsuta@eps.s.u-tokyo.ac.jp)

9 **Key Points:**

- 10 • The baroclinic energy conversion dissipates 55% of the local wind energy input within
11 the standing meander region.
- 12 • The vertical eddy energy flux redistributes the eddy kinetic energy in vertical within the
13 standing meander region.
- 14 • The eddy effects are negligible outside the standing meander region.

15

16 **Abstract**

17 Recent studies suggest that local eddy-mean flow interactions associated with standing
18 meanders play key roles in the dynamics of the Antarctic Circumpolar Current. Here we explore
19 the importance of the local dynamics quantitatively with a viewpoint of energy transfer using the
20 Lorentz diagram concept. Results confirm the importance of the eddy-mean flow interactions in
21 the standing meander, showing that 55% of the wind energy input is converted to the eddy
22 energy through the baroclinic instability in the standing meander region. It is also found that
23 most of the eddy kinetic energy is dissipated local in the deeper layer due to the vertical energy
24 redistribution governed by the vertical pressure flux. Contrary, the eddy effects are negligible
25 outside the standing meander region.

26 **Plain Language Summary**

27 The insensitivity of the Antarctic Circumpolar Current transport to changes in wind stress is
28 thought to be caused by a secondary circulation due to mesoscale eddies. Previous studies have
29 pointed out qualitatively that the eddy-mean flow interactions occur rather limited region near
30 standing meanders, but its quantitative evaluation of associated processes has not been
31 conducted. This study thus explores the importance of the local dynamics quantitatively using
32 the Lorentz diagram concept. Our results indicate that the baroclinic instability efficiently
33 transfer the wind energy input to the eddy energy within the standing meander regions. Only five
34 major standing meanders can provide most of the baroclinic energy transfer for the entire
35 Southern Ocean. It is also shown that the vertical pressure flux is responsible for the vertical
36 energy transport from the eddy energy generation sites in the upper 3000 m depth down to the
37 deeper layer, where the eddy energy dissipation mainly occurs.

38 1 Introduction

39 It has been suggested that total time-mean volume transport of the Antarctic Circumpolar
40 Current (ACC) and associated local meridional overturning circulation is insensitive to changes
41 in wind forcing (e.g. Hogg et al. 2008; Munday et al. 2013; Thompson and Naveira Garabato
42 2014; Constantinou and Hogg 2019). This phenomenon often referred to as “eddy saturation” is
43 explained through a balance between the wind-driven Ekman transport and the eddy-induced
44 counter transport in the zonally averaged framework (e.g. Marshall and Radko 2003; Marshall
45 and Speer 2012; Munday et al. 2013; Youngs et al. 2019). This zonally averaged view, however,
46 conceals the ACC’s complex frontal structures and eddy characteristics in the zonal direction
47 (Thompson and Naveira Garabato 2014 and references therein, hereafter TG2014). For example,
48 TG2014 suggested that large eddy activities are localized in the vicinity of standing meanders
49 associated with the significant topography and that eddy-mean flow interactions are quite weak
50 in the regions far from the standing meanders. Their analysis based on the Eliassen-Palm tensor
51 (Plumb, 1986) revealed that the eddy forcing along the streamlines decelerates the mean flow
52 within the meandering sections in the equilibrium state. TG2014 also showed that the increased
53 transport driven by the wind forcing enhances the meander curvature, resulted in enhanced eddy
54 kinetic energy (EKE). The large eddy activities strengthen the vertical momentum transport due
55 to baroclinic instability, which in turn changes the baroclinic structure of the meander and
56 decreases the mean flow. They indicated qualitative importance of this localized negative
57 feedback mechanism in the eddy saturation and suggested necessity of a quantitative evaluation
58 of the process.

59 Here we explore the importance of the local dynamics quantitatively with the viewpoint
60 of the Lorentz diagram concept (Lorentz, 1955). Although the eddy-mean flow energy transfer

61 over the entire Southern Ocean has already been analyzed in several previous literatures with
62 realistic models (Chen et al., 2014; Wu et al., 2017; Jüling et al., 2018), suggesting that
63 baroclinic instability dominates the generation of EKE, its spatial structure has not been
64 investigated. On the other hand, Youngs et al. (2017) has shown that the mixed barotropic and
65 baroclinic instability is important in the region of standing meanders using an idealized model,
66 but not for a realistic condition. In this study, detailed energy transfer, including the vertical
67 component of energy flux, is investigated using the local Lorentz diagram applied to the standing
68 meander region appeared in a realistic eddy-resolving model. Our results support the importance
69 of the local negative feedback hypothesis suggested by TG2014 and, in addition, give a clearer
70 insight into vertical energy redistribution associated with the eddy-mean flow interactions, which
71 is missing from the canonical Lorentz diagram analysis.

72

73 **2 Model Data**

74 Results from an eddy-resolving Ocean General Circulation Model (OGCM), named
75 OGCM for the Earth Simulator (OFES) (Masumoto et al., 2004), are used in the following
76 analyses. OFES is based on the Modular Ocean Model ver. 3 (MOM3) developed at GFDL
77 (Pacanowski & Griffies, 2000) and optimized for the massively-parallel computational
78 architecture of the Earth Simulator. The horizontal grid spacing is $0.1^\circ \times 0.1^\circ$ and there are 54
79 vertical levels. The 3-day snapshots for a period of 2001-2010, driven by the NCEP reanalysis
80 products as the surface boundary forcing, are used (see Sasaki et al. (2006, 2008) for more
81 detailed model settings). It has been shown that OFES captures variability in the Southern Ocean
82 realistically (e.g. Masumoto, 2010; TG2014), providing a reasonable platform to examine the

83 eddy-mean flow interactions in the ACC. It is confirmed that following results are qualitatively
 84 the same for different analysis periods.

85

86 **3 Method**

87 We consider a variable x that can be described by its temporal average \bar{x} and eddy
 88 perturbations x' as a deviation from the temporal average, i.e.,

$$89 \quad x' = x - \bar{x}. \quad (1)$$

90 With this separation between the mean field and eddy turbulences, the mean kinetic and
 91 available potential energy are respectively defined as

$$92 \quad K_M = \frac{1}{2} \rho_0 (\bar{u}^2 + \bar{v}^2), \quad (2)$$

$$93 \quad P_M = -\frac{1}{2} \frac{g}{n_0} \overline{\rho^{*2}}, \quad (3)$$

94 and the eddy kinetic energy (EKE) and the eddy available potential energy are defined as

$$95 \quad K_E = \frac{1}{2} \rho_0 (\overline{u'^2} + \overline{v'^2}), \quad (4)$$

$$96 \quad P_E = -\frac{1}{2} \frac{g}{n_0} \overline{\rho'^2}. \quad (5)$$

97 Here, n_0 is the globally averaged, time mean vertical gradient of the potential density referenced
 98 to a depth of 2000 m (Von Storch et al., 2012). The variation of the density is defined by

$$99 \quad \rho^* = \rho - \langle \bar{\rho} \rangle, \quad (6)$$

100 where $\langle \bar{X} \rangle$ means the temporal and global average of the value X .

101 According to Chen et al., (2014), the mean flow and eddy energy equations satisfy

$$102 \quad \begin{aligned} & \frac{\partial}{\partial t} K_M + \nabla(\bar{\mathbf{u}}K_M) + \rho_0 \nabla(\overline{u'u'} + \overline{v'v'}) + \nabla(\bar{\mathbf{u}}\bar{p}^*) \\ & = -g\overline{\rho^*w} - \rho_0[-\overline{u'u'} \cdot \nabla\bar{u} - \overline{v'v'} \cdot \nabla\bar{v}] + S(K_M), \end{aligned} \quad (7)$$

$$103 \quad \begin{aligned} & \frac{\partial}{\partial t} K_E + \nabla\left(\bar{\mathbf{u}}K_E + \overline{\mathbf{u}' \frac{1}{2}\rho_0(u'^2 + v'^2)}\right) + \nabla(\bar{\mathbf{u}}\bar{p}') \\ & = -g\overline{\rho'w'} + \rho_0[-\overline{u'u'} \cdot \nabla\bar{u} - \overline{v'v'} \cdot \nabla\bar{v}] + S(K_E) \end{aligned} \quad (8)$$

$$104 \quad \frac{\partial}{\partial t} P_M + \nabla(\bar{\mathbf{u}}P_M) + \nabla_h \cdot \left(-\overline{\rho'\mathbf{u}'_h} \frac{g}{n_0} \bar{\rho}^*\right) = g\overline{\rho^*w} - \frac{g}{n_0} \overline{\rho'\mathbf{u}'_h} \cdot \nabla_h \bar{\rho} + S(P_M), \quad (9)$$

$$105 \quad \frac{\partial}{\partial t} P_E + \nabla(\bar{\mathbf{u}}P_E) + \nabla \cdot \left(-\frac{g}{2n_0} \overline{\mathbf{u}'\rho'^2}\right) = g\overline{\rho'w'} + \frac{g}{n_0} \overline{\rho'\mathbf{u}'_h} \cdot \nabla_h \bar{\rho} + S(P_E), \quad (10)$$

106 where \mathbf{u} is the three-dimensional velocity vector, \mathbf{u}_h is the horizontal component of the velocity,
 107 ∇ is the three-dimensional gradient operator, ∇_h is the horizontal gradient operator, p is the
 108 combined sea surface elevation and hydrostatic pressure, $p^* = p - \langle \bar{p} \rangle$, $S(\cdot)$ is the source/sink
 109 term calculated as the residual from the respective balance equation. The second term of the right-
 110 hand side in the equations (7) and (8), i.e.

$$111 \quad BTR = \rho_0[-\overline{u'u'} \cdot \nabla\bar{u} - \overline{v'v'} \cdot \nabla\bar{v}], \quad (11)$$

112 is the barotropic conversion rate (BTR) due to eddy-mean flow interactions. Positive values of
 113 BTR means that the barotropic instability transfers the mean flow energy into the EKE.

114 Similarly, the second term of the right-hand side of the equations (9) and (10), i.e.

$$115 \quad BCR = \frac{g}{n_0} \overline{\rho'\mathbf{u}'_h} \cdot \nabla_h \bar{\rho}, \quad (12)$$

116 is the baroclinic conversion rate (BCR), whose positive sign indicates that eddies extract the
 117 mean available potential energy from the mean stratification. The first term of the right-hand side
 118 of the equation (8) and (10), i.e.

$$119 \quad VEDF = -g\overline{\rho'w'},$$

120 is the vertical eddy density flux (VEDF), which releases the eddy available potential energy
 121 generated due to baroclinic instability. Positive values of the VEDF are associated with the
 122 convective process, with dense fluid sinking and light fluid rising (Zhai & Marshall, 2013; Aiki
 123 et al., 2016). The third term of the left-hand side of (8), i.e. $\nabla \cdot (\overline{\mathbf{u}'p'})$, is the energy flux by the
 124 eddy pressure work, of which the vertical component $\partial_z(\overline{w'p'})$ represents redistribution of the
 125 EKE in vertical (Zhai & Marshall, 2013).

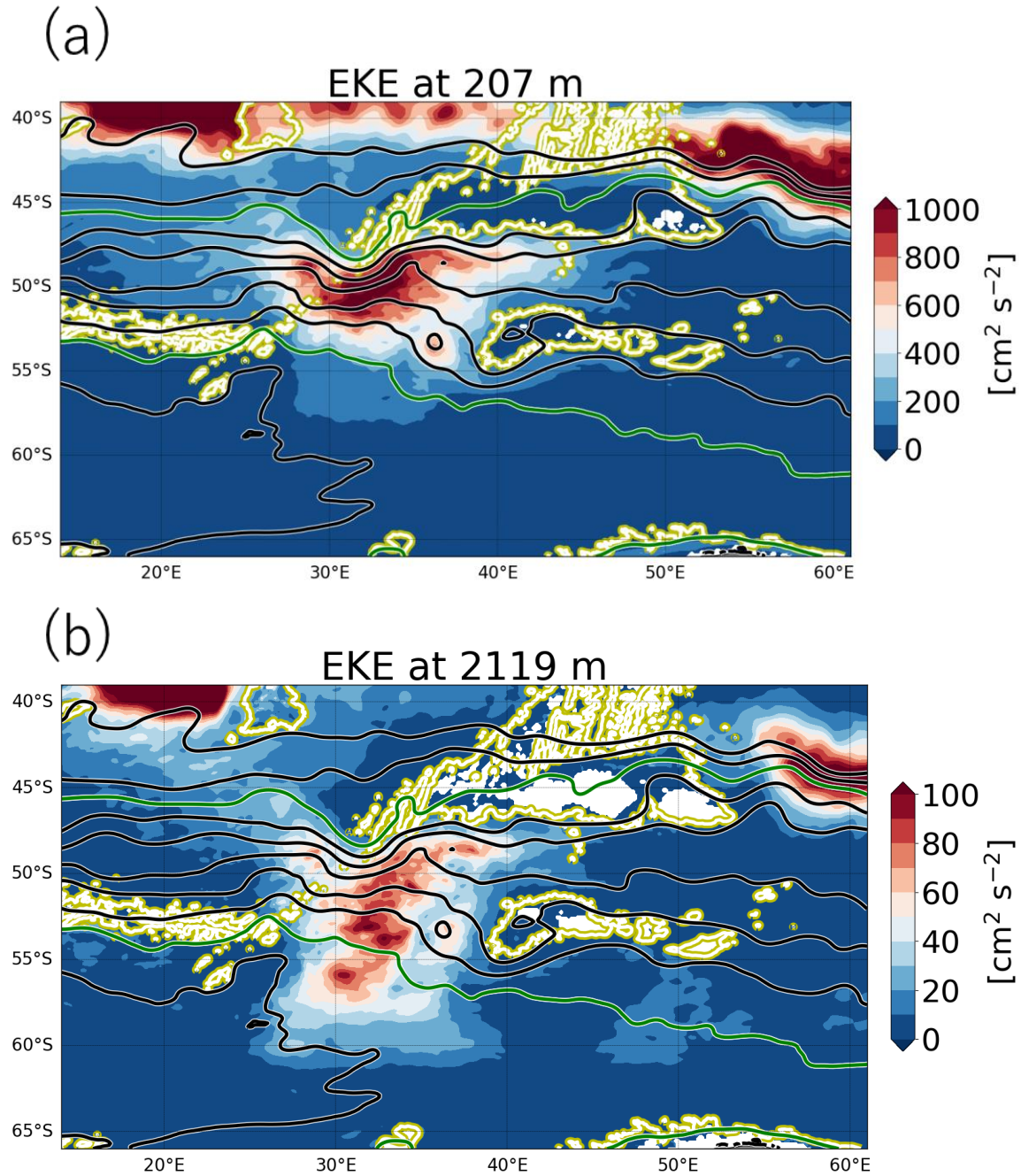
126 Noted here that the available potential energies in the form of (3) and (5) are not the
 127 exact conservative quantities (Von Storch et al., 2012; Chen et al., 2014; Aiki et al., 2016), and
 128 resultant conservation equations of (9) and (10) are the approximate forms (Chen et al., 2014;
 129 Aiki et al., 2016; Wu et al., 2017). Aiki et al. (2016) proposed the exact form of the eddy
 130 available potential energy, independent of the choice of the background density profile, without
 131 any assumptions and derived the associated conservation law. However, their eddy available
 132 potential energy is not well-defined in the mixed-layer and inside the weakly stratified water
 133 mass such as the Subantarctic Mode Water (McCartney, 1979). Therefore, we use the
 134 approximated energy equations of (7) - (10) in the present study. It should be noted here,
 135 however, that our results do not change qualitatively when we use the exact Lorentz diagram of
 136 Aiki et al. (2016).

137 **4 Results**

138 4.1 Basic structures of the standing meander

139 We focus on the standing meander of the ACC in the region 45°S - 60°S, 25°E - 40°E in
140 this study. This choice is arbitrary, but resultant energy pathways in other standing meanders are
141 almost the same (see the supplement materials). Horizontal distributions of the EKE in the upper
142 layer at a depth of 207 m and the sea surface elevation averaged from 2001 to 2010 simulated in
143 OFES are shown in Figure 1a. The strong eastward flow associated with the ACC is mainly
144 located within a region bounded by the sea surface elevation contours of -0.4 m and -1.6 m.
145 The contours of the sea surface elevation are closely packed in the upstream region (west of
146 35°E), while downstream of the meander (east of 35°E) the ACC jet broadens. Inside the
147 meander, the EKE values exceed $1000 \text{ cm}^2 \text{ s}^{-2}$. Regions of relatively large EKE values are also
148 observed along the 3000 m isobath between 40°E and 50°E in spite of the weak sea surface
149 elevation gradient. On the other hand, the EKE is very weak far from the standing meander
150 region, indicating non-uniformity of the ACC in the zonal direction. The horizontal distribution
151 of the EKE in the deeper layer at a depth of 2119 m (Figure 1b) has a coherent structure with that
152 of the surface EKE. The EKE values are larger than $80 \text{ cm}^2 \text{ s}^{-2}$ within the longitude band of the
153 standing meander, while they are smaller than $20 \text{ cm}^2 \text{ s}^{-2}$ outside the standing meander. All
154 these features of the EKE are consistent with the previous studies (e.g. TG2014 and references
155 therein).

156



157

158 Figure 1. Horizontal distributions of the EKE at a depth of (a) 207 m and (b) 2119 m. Black and
159 green contours in (a) represent the sea surface elevation with a contour interval of 0.2 m, with
160 green lines indicate the -0.4 m and -1.6 m contours as the boundaries of the ACC. The yellow-
161 edged white contours indicate the 3000 m isobath.

162

163 4.2 Horizontal distribution of the energy conversion rate

164 Figure 2 shows spatial distributions of the mean wind energy input, the BTR, and the
165 VEDF. The mean wind energy input is calculated using $W_{wind} = \bar{\tau} \cdot \bar{\mathbf{u}}_0$, where $\bar{\tau}$ is the mean
166 surface wind stress and $\bar{\mathbf{u}}_0$ is the mean total surface velocity (Zhai & Marshall, 2013). Since the
167 BCR includes the rotational component which doesn't contribute to the eddy-mean flow energy
168 transfer (Marshall & Shutts, 1981), it would be useful to examine the VEDF as the baroclinic
169 energy pathway instead (Chen, 2013). According to Figure 2a, the surface wind forcing is
170 uniformly distributed along the ACC path. The westerlies are as high as 0.2 N m^{-2} between the
171 sea surface elevation contours of -0.4 m and -1.6 m . Reflecting the homogeneous distribution
172 of wind stress, the energy input is also large in a wide area within the ACC, exceeding
173 $4.0 \times 10^{-2} \text{ W m}^{-2}$. The atmospheric winds thus tend to homogeneously accelerate the ACC.

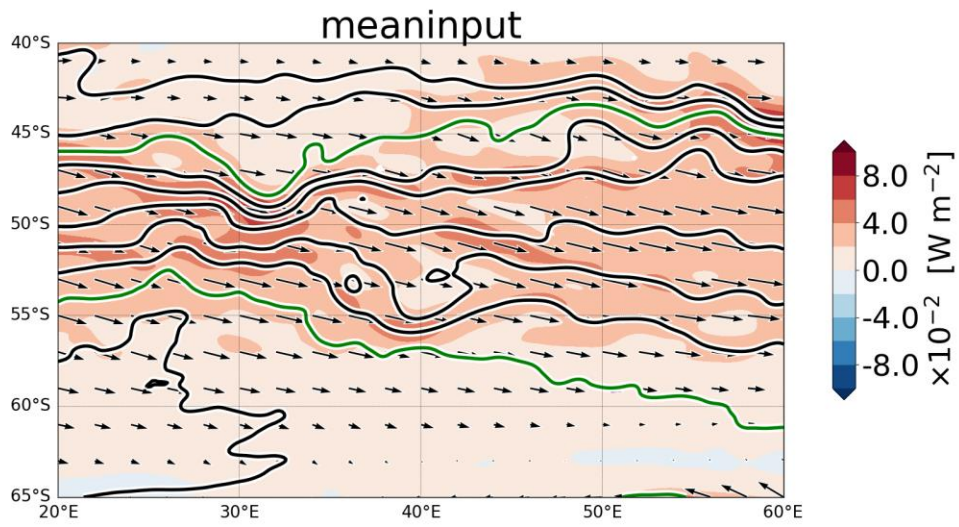
174 On the other hand, large values of the BTR and VEDF are highly confined in the standing
175 meander region, bounded by the 25°E and 40°E longitude lines zonally and by -0.4 m and
176 -1.6 m sea surface elevation contours meridionally (SM region hereafter) (Figure 2b,c). The
177 elongated dipole structures of the BTR are observed in the region $47^\circ\text{S} - 50^\circ\text{S}$, $33^\circ\text{E} - 38^\circ\text{E}$, where
178 the contours of sea surface elevation are densely packed together. The area-integrated BTR in the
179 SM region is 0.2 GW , which is only 0.5% of the wind energy input, indicating that the
180 barotropic instability plays a minor role in the dynamics in the standing meander. Unlike the
181 BTR, the VEDF (Figure 2c) is uniformly large inside the SM region, suggesting that eddies
182 systematically work to flatten isopycnals. As is expected from the linear theory of the baroclinic
183 instability (e.g. Olbers et al. 2012), the EKE generation through the VEDF follows the location

184 of the mean sea surface elevation gradients. Values of the VEDF exceeds $8.0 \times 10^{-2} \text{ W m}^{-3}$ at
185 around the center of the standing meander and larger than $4.0 \times 10^{-2} \text{ W m}^{-3}$ at the flank of the
186 jet. The area-integrated value of the VEDF in the SM region reaches 21 GW, which is nearly
187 55% of the local mean wind energy input. This result is consistent with previous works using
188 realistic eddy-resolving models (Zhai & Marshall, 2013; Aiki et al., 2016), which has shown that
189 the wind energy input to the gyre circulation is largely balanced by the VEDF. It is also worth
190 noting that this VEDF distribution differs slightly from that of the EKE distribution (Figure 1).
191 The eddy production is larger between 25°E and 35°E compared to that in the region east of 35°E
192 even within the SM region, whereas relatively large values of the EKE extend to the east of
193 35°E . The area-integrated EKE advection i.e. $\nabla(\overline{\mathbf{u}K_E})$ in the eastern part of SM region between
194 35°E and 40°E is 3.0 GW, which is comparable to the VEDF value of 3.8 GW within the same
195 region, suggesting that transient eddies are advected downstream from a region of the initial
196 baroclinic growth as pointed out in previous researches (Abernathey & Cessi, 2014; Bischoff &
197 Thompson, 2014; Thompson & Garabato, 2014; Chapman et al., 2015; Youngs et al., 2017).

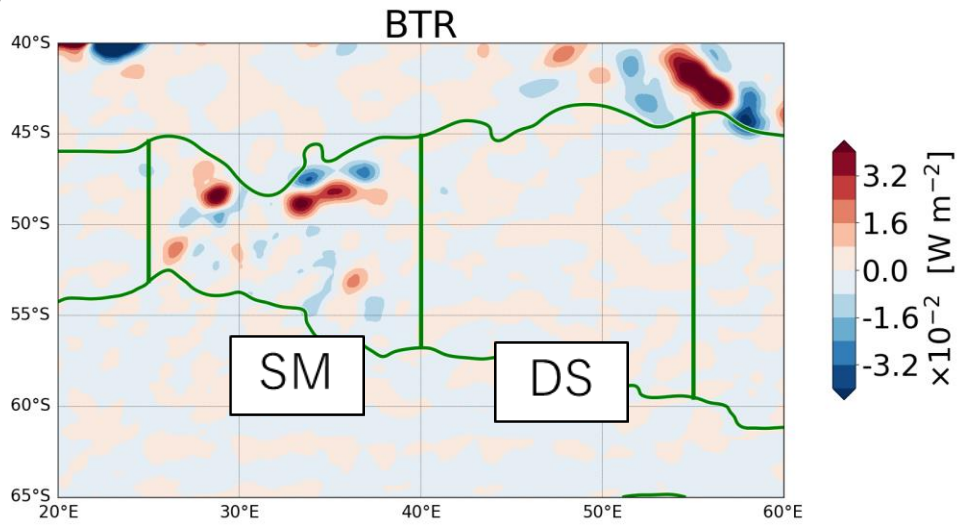
198 In the downstream region, bounded by the 40°E and 55°E longitude lines zonally and
199 -0.4 m and -1.6 m sea surface elevation contours meridionally (DS region hereafter) (see
200 Fig.2b for the location), the baroclinic conversion is weak in spite of the strong energy input by
201 the wind forcing. While the wind energy input is 44 GW in the DS region, the value of VEDF is
202 only 1.6 GW. The barotropic conversion also has little contributions to the EKE balances. These
203 features demonstrate that the energy cascade by eddy-mean flow interactions is localized within
204 the SM region, which is consistent with the result of TG2014.

205

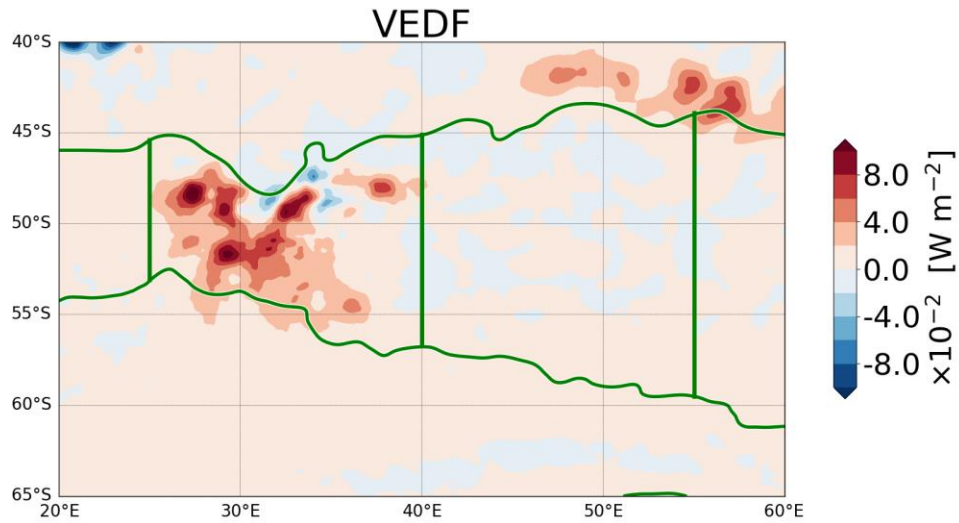
(a)



(b)



(c)



207

208 Figure 2. Horizontal distributions of (a) the mean wind energy input, (b) the BTR, and (c) the
 209 VEDF. The black arrows in (a) represent the mean wind stress. The black and green contours in
 210 (a) are the same as those in Figure 1. The region bounded by two green contours representing the
 211 northern and southern boundaries of the ACC is further divided into the standing meander (SM)
 212 region and the downstream (DS) region by 25°E, 40°E, and 55°E longitude lines and shown in
 213 (b) and (c).

214

215

216 The Lorentz diagram shown in Figure 3 summarizes more detailed energy pathways,
217 including the energy transfer discussed above, focusing on the eddy energy budget. It is noted
218 that non-local eddy-mean flow interactions (Murakami, 2011; Chen et al., 2014, 2016) is
219 confirmed to be negligible in our target region, therefore we don't treat the non-local interactions
220 in this paper. The baroclinic conversion rate BCR in the SM region is as large as 22 GW , which
221 is nearly equal to that of the VEDF. This large values of the BCR suggest that the eddy induced
222 density transport effectively runs across the mean density contours and weakens the isopycnal
223 slope. Almost all the extracted energy by the baroclinic instability is released from the
224 stratification through the VEDF as seen in the above discussion. Since the barotropic energy
225 conversion rate and advective fluxes are weak in the SM region, almost all the converted EKE
226 through the baroclinic instability is dispersed locally by the viscosity and the bottom drag. On the
227 other hand, the energy sink in the form of the eddy available potential energy is only 1.6 GW.
228 Therefore, more than a half of the local energy input by the winds is dissipated through the
229 baroclinic energy pathway $P_M \rightarrow P_E \rightarrow K_E$ in the SM region, which is similar to the energy
230 pathway obtained for the entire ACC region (Chen et al. 2014; Wu et al. 2017; Jüling et al. 2018
231 and Supplement in this paper).

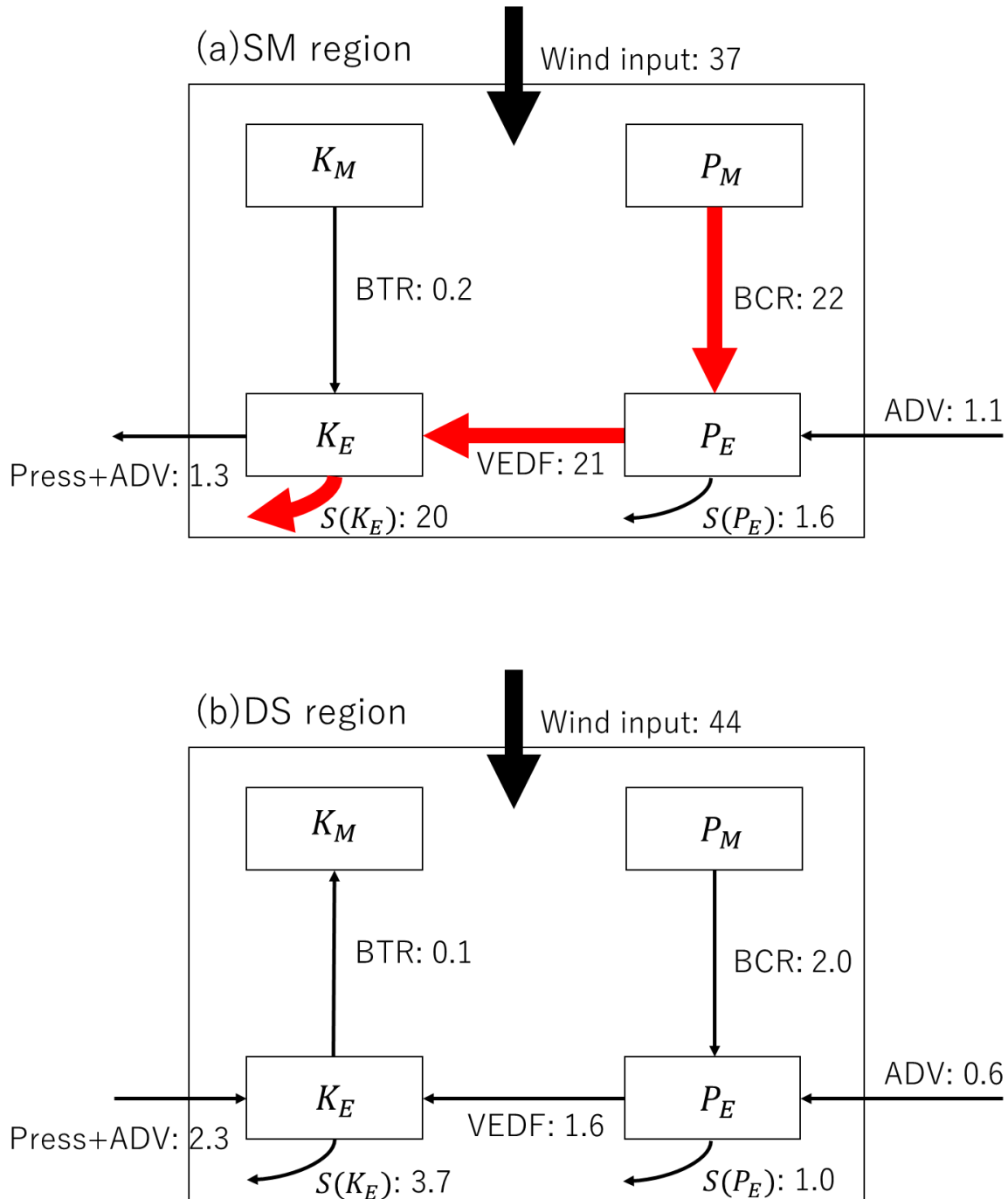
232 In the DS region, on the other hand, the baroclinic conversion rate is very small, while
233 the wind input is comparable to that in the SM region. Only 5% of the energy gain is cascaded to
234 the eddy fields, indicating that the energy sink by the eddy-mean flow interactions is localized in
235 the SM region. This result suggests that a limited area of the ACC showing the standing meander
236 is possibly responsible for the baroclinic energy pathway of the entire Southern Ocean as
237 hypothesized by TG2014. In fact, the VEDF (the EKE dispersion) integrated in the five major

238 standing meander regions along the ACC reaches 74% (67%) of the VEDF (the EKE dispersion)

239 integrated over the entire ACC (see Supplement).

240

241



242

243 Figure 3. The Lorentz energy diagram in GW (10^9 W) calculated in the SM region (upper

244 diagram) and the DS region (lower diagram), respectively. Black and red arrows connecting the

245 four boxes represent the energy transfer associated with the barotropic conversion (BTR), the
246 baroclinic conversion (BCR), and the vertical eddy density flux (VEDF). The curved arrow of
247 $S(K_E)$ ($S(P_E)$) connected to the K_E (P_E) box indicates the energy source/sink in the equation (8)
248 (the equation (10)).
249

250

251 4.3 The vertical energy transfer

252 Figure 4 shows vertical distributions of the VEDF, source/sink of the EKE i.e. $S(K_E)$ of
253 (8), divergence of the eddy pressure flux $\nabla(\overline{\mathbf{u}'p'})$, and its difference from the vertical component
254 $\partial_z(\overline{w'p'})$. Each value is obtained by averaging over the meridional extent of the envelope
255 bounded by the -0.4 m and -1.6 m sea surface elevation contours. This choice of the
256 boundaries is arbitrary, but following results do not change with a different choice of bounded
257 contours.

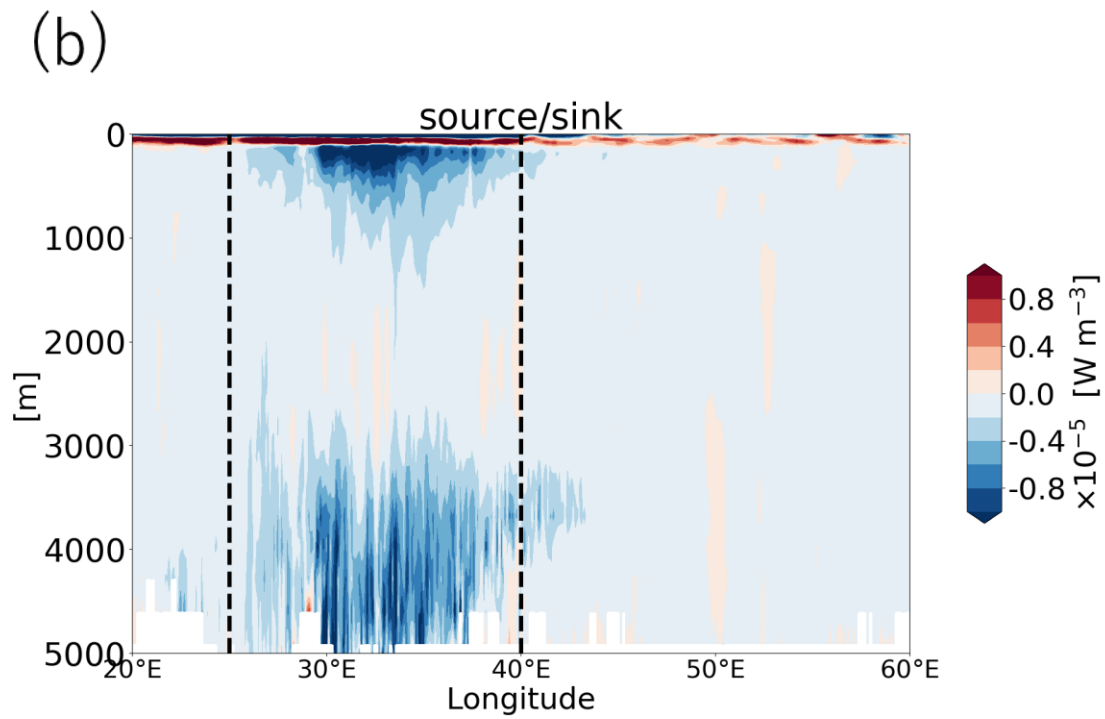
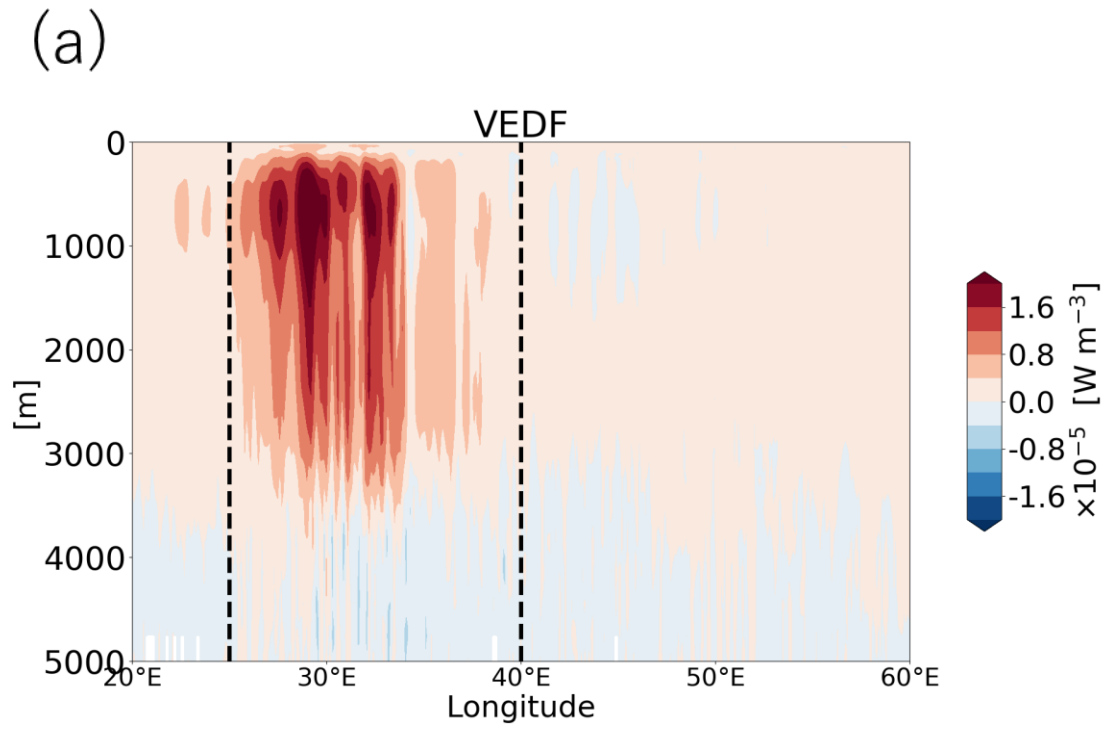
258 According to Figure 4a, the EKE generation has a deep structure with its maximum
259 strength in the upper 1000 m depth and relatively strong values penetrate down to a depth deeper
260 than 3000 m. This feature is different from the vertical structure of VEDF in both the subtropical
261 gyre, where the large VEDF is surface-intensified, and the subpolar gyre, where the maximum of
262 VEDF appears around a depth of 2000 m, in the North Atlantic (Zhai & Marshall, 2013). The
263 zonal position of the active eddy generation area follows the location of the standing meander.
264 Although the VEDF is relatively small in the eastern part of the SM region ($35^\circ\text{E} - 40^\circ\text{E}$), it has
265 also a deep structure reaching a depth of 3000 m.

266 The distribution of the source/sink terms (Figure 4b) is different from that of the VEDF.
267 Strong EKE dissipation, i.e. the energy sink, are observed within the upper 500 m depth or the
268 layer below 3000 m depth in the SM region. This mismatch in the vertical location between the
269 energy generation and the energy sink can be reconciled through the non-local process by the
270 pressure flux (Figure 4c). While the energy flux by the pressure work converges in the lower
271 layer deeper than 3000 m depth, it diverges in the upper 3000 m depth, where the EKE

272 production is prominent as seen in Figure 4a. This vertical communication seems to be achieved
273 by the vertical pressure flux $\overline{w'p'}$, which shows downward flux throughout the water column
274 east of 30°E. The eddy energy flux thus acts to make the flow more barotropic inside the
275 standing meander. In the region west of 30°E, the vertical pressure flux is upward near the
276 surface and downward in the deeper layer with the separation boundary at around 2000 m depth.
277 This upward flux in the upper layer of the upstream region may be related to the increase in the
278 baroclinicity of the flow by the along-stream eddy forcing shown in TG2014. To confirm that the
279 vertical communication is dominated by the vertical energy flux, we calculate the difference
280 between $\nabla(\overline{\mathbf{u}'p'})$ and $\partial_z(\overline{w'p'})$ (Figure 4d). The difference is quite small in the layer below 1000
281 m depth, although there are signatures of small-scale noises in the depth below 4000 m depth.
282 Therefore, it is concluded that the EKE is generated in the upper 3000 m depth and the eddy
283 energy is transported downward by the vertical pressure flux. The eddy energy converged near
284 the bottom may be dissipated by the bottom friction and the viscosity in OFES. In reality,
285 energy dissipation associated with small-scale processes, such as the generation of internal
286 waves by the topography, may be important as the energy sink.

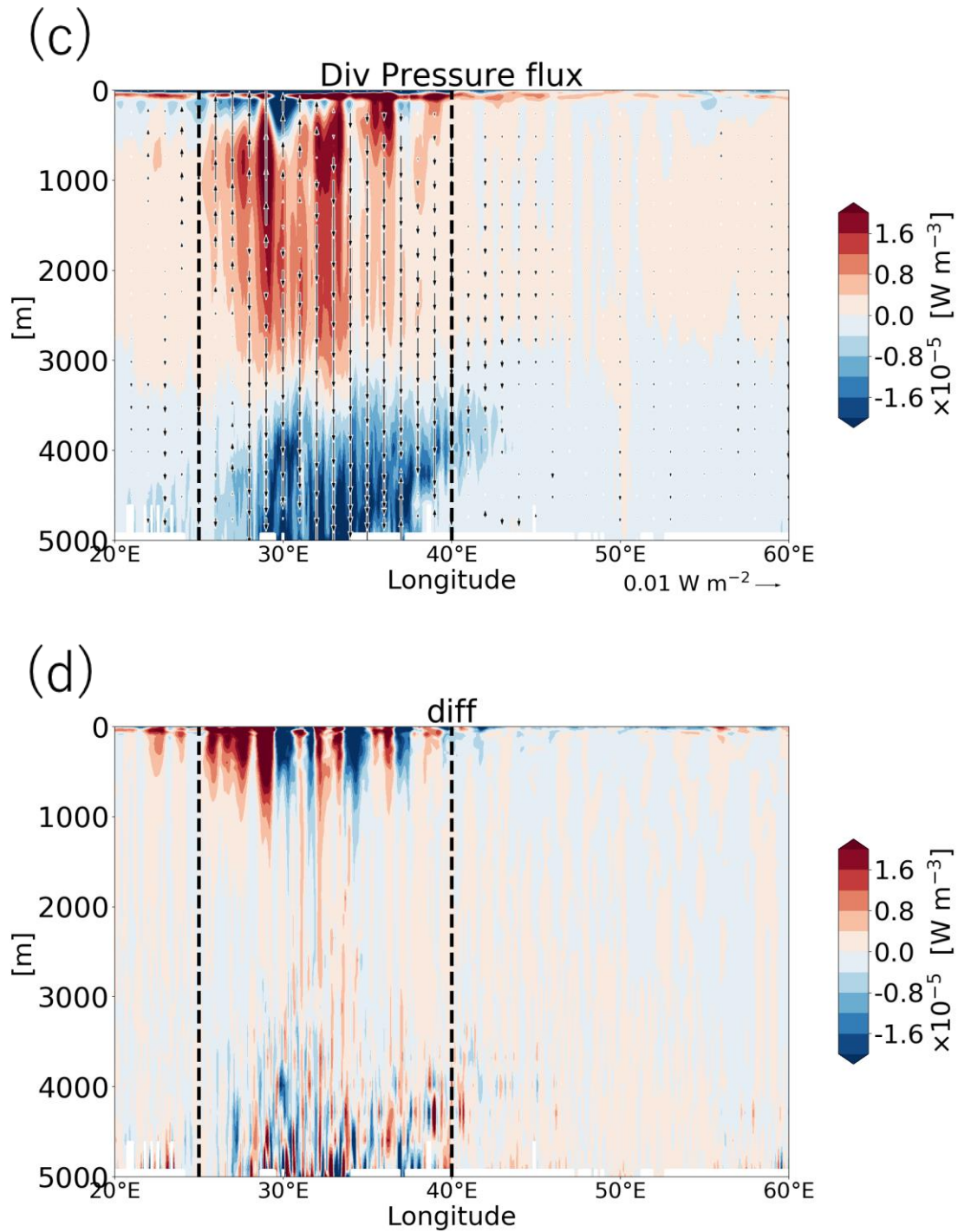
287

288



289

290



291

292 Figure 4. The vertical distribution of (a) the VEDF, (b) the eddy energy sources/sinks, (c) the

293 divergence of the pressure flux $\nabla(\overline{\mathbf{u}'p'})$, and (d) the differences between the divergence of the

294 pressure flux and its vertical component $\partial_z(\overline{w'p'})$ averaged meridionally in the envelope defined
295 by -0.4m and -1.6m seas surface elevation contours. The black arrows in (c) represent the
296 vertical energy flux $\overline{w'p'}$ in $W m^{-2}$. The vertical black dotted lines at 25°E and 40°E indicate the
297 western and eastern boundary of the standing meander region, respectively.
298

299

300 **5 Discussion and Conclusions**

301 We have evaluated the energy pathways and the role of vertical energy flux in the
302 standing meander region of the ACC using outputs of an eddy resolving OGCM from the
303 viewpoint of the eddy-mean flow interactions. The analysis of the Lorentz diagram reveals that
304 more than a half of the wind energy input is converted to the eddy energy through the baroclinic
305 conversion $P_M \rightarrow P_E \rightarrow K_E$ in the standing meander region. In the downstream region, the wind
306 energy input has the same magnitude as that in the standing meander region, whereas the eddy-
307 mean flow interactions no longer work efficiently. The eddy kinetic energy generation occurs
308 mainly in the layer shallower than 3000 m depth. It is the vertical pressure flux that transport the
309 EKE from the generation sites to the deeper layer, where the energy dissipation mainly occurs.
310 The pressure flux, therefore, plays a key role for the vertical energy redistribution although it is
311 shown to have only a minor role in the integrated viewpoint of the Lorentz diagram (see
312 Supplement for the schematic map of our findings).

313 These results suggest that the eddy-mean flow interactions in the standing meander
314 region play a significant role in relaxing changes in the wind forcing. In fact, the dissipation of
315 EKE integrated only in the five major meanders reaches 22% of the total mean wind energy
316 input and 67% of the EKE dissipation over the entire ACC region (see Supplement), supporting
317 importance of the local negative-feedback mechanism of the eddy saturation suggested in
318 TG2014.

319 The energy dissipation except for the standing meander regions is a remaining problem.
320 Although the baroclinic conversion rate can balance the local wind forcing, it is insufficient to

321 dissipate all the energy gained over the entire ACC. Recently, Youngs et al. (2019) suggested
322 using the two-layer quasigeostrophic channel model that the residual overturning circulation is
323 also important for the eddy saturation as well as the processes associated with a topography.
324 Armour et al. (2016) showed that the surface heat advection may also contribute to the energy
325 export from the Southern Ocean, although their model is too coarse to resolve eddy effects. Since
326 the energy pathways in the idealized model could be different from that in the realistic model,
327 these mechanisms should be tested using outputs of realistic eddy-resolving models. The
328 estimation of the three-dimensional residual circulation in a realistic OGCM is challenging and
329 needs further investigation.

330

331

332 **Acknowledgments**

333 This work was supported by a JSPS Grant-in-Aid for Scientific Research(A) (17H01663) and a
334 JSPS Grant-in-Aid for Transformative Research Areas(B) (20H05731). OFES data and its
335 information are available in <http://www.jamstec.go.jp/datadoi/doi/10.17596/0002029.html>.

336

337 **References**

338 Abernathey, R., & Cessi, P. (2014). Topographic enhancement of Eddy efficiency in baroclinic
339 equilibration. *Journal of Physical Oceanography*, *44*(8), 2107–2126.

340 <https://doi.org/10.1175/JPO-D-14-0014.1>

341 Aiki, H., Zhai, X., & Greatbatch, R. J. (2016). Energetics of the global ocean: The role of
342 mesoscale eddies. *World Scientific Series on Asia-Pacific Weather and Climate*, *7*, 109–
343 134. https://doi.org/10.1142/9789814696623_0004

344 Armour, K. C., Marshall, J., Scott, J. R., Donohoe, A., & Newsom, E. R. (2016). Southern Ocean
345 warming delayed by circumpolar upwelling and equatorward transport. *Nature Geoscience*,

346 *9*(7), 549–554. <https://doi.org/10.1038/ngeo2731>

347 Bischoff, T., & Thompson, A. F. (2014). Configuration of a Southern Ocean storm track. *Journal*
348 *of Physical Oceanography*, *44*(12), 3072–3078. <https://doi.org/10.1175/JPO-D-14-0062.1>

349 Chapman, C. C., Hogg, A. M. C., Kiss, A. E., & Rintoul, S. R. (2015). The dynamics of
350 Southern Ocean storm tracks. *Journal of Physical Oceanography*, *45*(3), 884–903.

351 <https://doi.org/10.1175/JPO-D-14-0075.1>

- 352 Chen, R. (2013). Energy pathways and structures of oceanic eddies from the ECCO2 state
353 estimate and simplified models. *Energy Pathways and Structures of Oceanic Eddies from*
354 *the ECCO2 State Estimate and Simplified Models*. <https://doi.org/10.1575/1912/5793>
- 355 Chen, R., Flierl, G. R., & Wunsch, C. (2014). A description of local and nonlocal eddy-mean
356 flow interaction in a global eddy-permitting state estimate. *Journal of Physical*
357 *Oceanography*, *44*(9), 2336–2352. <https://doi.org/10.1175/JPO-D-14-0009.1>
- 358 Chen, R., Thompson, A. F., & Flierl, G. R. (2016). Time-dependent eddy-mean energy diagrams
359 and their application to the ocean. *Journal of Physical Oceanography*, *46*(9), 2827–2850.
360 <https://doi.org/10.1175/JPO-D-16-0012.1>
- 361 Constantinou, N. C., & Hogg, A. M. C. (2019). Eddy Saturation of the Southern Ocean: A
362 Baroclinic Versus Barotropic Perspective. *Geophysical Research Letters*, *46*(21), 12202–
363 12212. <https://doi.org/10.1029/2019GL084117>
- 364 Firing, Y. L., Chereskin, T. K., & Mazloff, M. R. (2011). Vertical structure and transport of the
365 Antarctic Circumpolar Current in Drake Passage from direct velocity observations. *Journal*
366 *of Geophysical Research: Oceans*, *116*(8), 1–16. <https://doi.org/10.1029/2011JC006999>
- 367 Hogg, A. M. C., Meredith, M. P., Blundel, J. R., & Wilson, C. (2008). Eddy heat flux in the
368 Southern ocean: Response to variable wind forcing. *Journal of Climate*, *21*(4), 608–620.
369 <https://doi.org/10.1175/2007JCLI1925.1>
- 370 Jüling, A., Viebahn, J. P., Drijfhout, S. S., & Dijkstra, H. A. (2018). Energetics of the Southern
371 Ocean Mode. *Journal of Geophysical Research: Oceans*, *123*(12), 9283–9304.
372 <https://doi.org/10.1029/2018JC014191>

- 373 Killworth, P. D. (1992). An Equivalent-Barotropic Mode in the Fine Resolution Antarctic
374 Model. *Journal of Physical Oceanography*, 22(11), 1379–1387.
375 [https://doi.org/10.1175/1520-0485\(1992\)022<1379:AEBMIT>2.0.CO;2](https://doi.org/10.1175/1520-0485(1992)022<1379:AEBMIT>2.0.CO;2)
- 376 Killworth, P. D., & Hughes, C. W. (2002). The antarctic circumpolar current as a free
377 equivalent-barotropic jet. *Journal of Marine Research*, 60(1), 19–45.
378 <https://doi.org/10.1357/002224002762341230>
- 379 Lorentz, E. N. (1955). Available Potential Energy and the Maintenance of the General
380 Circulation. *Tellus*, 7(2), 157–167. <https://doi.org/10.1111/j.2153-3490.1955.tb01148.x>
- 381 Marshall, J., & Radko, T. (2003). Residual-Mean Solutions for the Antarctic Circumpolar
382 Current and Its Associated Overturning Circulation. *Journal of Physical Oceanography*,
383 33(11), 2341–2354. [https://doi.org/10.1175/1520-0485\(2003\)033<2341:RSFTAC>2.0.CO;2](https://doi.org/10.1175/1520-0485(2003)033<2341:RSFTAC>2.0.CO;2)
- 384 Marshall, J., & Shutts, G. (1981). A Note on Rotational and Divergent Eddy Fluxes. *Journal of*
385 *Physical Oceanography*, 11(12), 1677–1680. [https://doi.org/10.1175/1520-0485\(1981\)011<1677:ANORAD>2.0.CO;2](https://doi.org/10.1175/1520-0485(1981)011<1677:ANORAD>2.0.CO;2)
- 386
- 387 Marshall, J., & Speer, K. (2012). Closure of the meridional overturning circulation through
388 Southern Ocean upwelling. *Nature Geoscience*, 5(3), 171–180.
389 <https://doi.org/10.1038/ngeo1391>
- 390 Masumoto, Y., Sasaki, H., Kagimoto, T., Komori, N., Ishida, A., Sasai, Y., et al. (2004). A fifty-
391 year eddy-resolving simulation of the world ocean: Preliminary outcomes of OFES (OGCM
392 for the Earth Simulator). *Journal of the Earth Simulator*, 1(January), 35–56. Retrieved from
393 http://www.jamstec.go.jp/esc/publication/journal/jes_vol.1/pdf/JES1-3.2-masumoto.pdf

- 394 McCartney, M. S. (1979). Subantarctic Mode Water. *Woods Hole Oceanographic Institution*
395 *Contribution*, 3773, 103–119. Retrieved from <http://oceanrep.geomar.de/48397/>
- 396 Munday, D. R., Johnson, H. L., & Marshall, D. P. (2013). Eddy saturation of equilibrated
397 circumpolar currents. *Journal of Physical Oceanography*, 43(3), 507–532.
398 <https://doi.org/10.1175/JPO-D-12-095.1>
- 399 Murakami, S. (2011). Atmospheric local energetics and energy interactions between mean and
400 eddy fields. Part I: Theory. *Journal of the Atmospheric Sciences*, 68(4), 760–768.
401 <https://doi.org/10.1175/2010JAS3664.1>
- 402 Olbers, D., Willebrand, J., & Eden, C. (2012). *Ocean Dynamics*. Berlin, Heidelberg: Springer
403 Berlin Heidelberg. <https://doi.org/10.1007/978-3-642-23450-7>
- 404 Pacanowski, R. C., & Griffies, S. M. (2000). MOM 3.0 Manual. *Geophys. Fluid Dyn. Lab., Natl.*
405 *Atmos. Admin., Princeton*, 682.
- 406 Plumb, R. A. (1986). Three-dimensional propagation of transient quasi-geostrophic eddies and
407 its relationship with the eddy forcing of the time-mean flow. *Journal of the Atmospheric*
408 *Sciences*. [https://doi.org/10.1175/1520-0469\(1986\)043<1657:TDPOTQ>2.0.CO;2](https://doi.org/10.1175/1520-0469(1986)043<1657:TDPOTQ>2.0.CO;2)
- 409 Sasaki, H., Sasai, Y., Nonaka, M., Masumoto, Y., & Kawahara, S. (2006). An Eddy-Resolving
410 Simulation of the Quasi-Global Ocean Driven by Satellite-Observed Wind Field
411 Preliminary Outcomes from Physical and Biological Fields. *Journal of Earth Simulator*,
412 6(October), 35–49. <https://doi.org/10.32131/jes.6.35>
- 413 Sasaki, H., Nonaka, M., Masumoto, Y., Sasai, Y., Uehara, H., & Sakuma, H. (2008). An Eddy-
414 Resolving Hindcast Simulation of the Quasiglobal Ocean from 1950 to 2003 on the Earth
415 Simulator. In *High Resolution Numerical Modelling of the Atmosphere and Ocean* (pp.

- 416 157–185). New York, NY: Springer New York. [https://doi.org/10.1007/978-0-387-49791-](https://doi.org/10.1007/978-0-387-49791-4_10)
417 4_10
- 418 Von Storch, J. S., Eden, C., Fast, I., Haak, H., Hernández-Deckers, D., Maier-Reimer, E., et al.
419 (2012). An estimate of the Lorenz energy cycle for the World Ocean based on the
420 1/10°STORM/NCEP simulation. *Journal of Physical Oceanography*, 42(12), 2185–2205.
421 <https://doi.org/10.1175/JPO-D-12-079.1>
- 422 Thompson, A. F., & Garabato, A. C. N. (2014). Equilibration of the Antarctic Circumpolar
423 Current by standing meanders. *Journal of Physical Oceanography*, 44(7), 1811–1828.
424 <https://doi.org/10.1175/JPO-D-13-0163.1>
- 425 Wu, Y., Wang, Z., & Liu, C. (2017). On the response of the Lorenz energy cycle for the
426 Southern Ocean to intensified westerlies. *Journal of Geophysical Research: Oceans*,
427 122(3), 2465–2493. <https://doi.org/10.1002/2016JC012539>
- 428 Youngs, M. K., Thompson, A. F., Lazar, A., & Richards, K. J. (2017). ACC meanders, energy
429 transfer, and mixed barotropic-baroclinic instability. *Journal of Physical Oceanography*,
430 47(6), 1291–1305. <https://doi.org/10.1175/JPO-D-16-0160.1>
- 431 Youngs, M. K., Flierl, G. R., & Ferrari, R. (2019). Role of residual overturning for the sensitivity
432 of southern ocean isopycnal slopes to changes in wind forcing. *Journal of Physical*
433 *Oceanography*, 49(11), 2867–2881. <https://doi.org/10.1175/JPO-D-19-0072.1>
- 434 Zhai, X., & Marshall, D. P. (2013). Vertical eddy energy fluxes in the North Atlantic subtropical
435 and subpolar gyres. *Journal of Physical Oceanography*, 43(1), 95–103.
436 <https://doi.org/10.1175/JPO-D-12-021.1>